

# Osmotic transport at the aqueous graphene and hBN interfaces: scaling laws from a unified, first principles description.

Laurent Joly,<sup>†,‡</sup> Robert H. Meißner,<sup>¶,§</sup> Marcella Iannuzzi,<sup>||</sup> and Gabriele Tocci<sup>\*,||</sup>

<sup>†</sup>*Univ Lyon, Univ Claude Bernard Lyon 1, CNRS, Institut Lumière Matière, F-69622, VILLEURBANNE, France*

<sup>‡</sup>*Institut Universitaire de France (IUF), 1 rue Descartes, 75005 Paris, France*

<sup>¶</sup>*Hamburg University of Technology, Institute of Polymers and Composites, Hamburg, 21073, Hamburg*

<sup>§</sup>*Helmholtz-Zentrum Hereon, Institute of Surface Science, Geesthacht, 21502, Germany*

<sup>||</sup>*Department of Chemistry, Universität Zürich, 8057 Zürich, Switzerland*

E-mail: gabriele.tocci@chem.uzh.ch

## Abstract

Osmotic transport in nanoconfined aqueous electrolytes provides new venues for water desalination and “blue energy” harvesting; the osmotic response of nanofluidic systems is controlled by the interfacial structure of water and electrolyte solutions in the so-called electrical double layer (EDL), but a molecular-level picture of the EDL is to a large extent still lacking. Particularly, the role of the electronic structure has not been considered in the description of electrolyte/surface interactions. Here, we report enhanced sampling simulations based on *ab initio* molecular dynamics, aiming at unravelling the free energy of prototypical ions adsorbed at the aqueous graphene and hBN interfaces, and its consequences on nanofluidic osmotic transport. Specifically, we predicted the zeta potential, the diffusio-osmotic mobility and the diffusio-osmotic conductivity for a wide range of salt concentrations from the *ab initio* water and ion spatial distributions through an analytical framework based on Stokes equation and a modified Poisson-Boltzmann equation. We observed concentration-dependent scaling laws, together with dramatic differences in osmotic transport between the two interfaces, in-

cluding diffusio-osmotic flow and current reversal on hBN, but not on graphene. We could rationalize the results for the three osmotic responses with a simple model based on characteristic length scales for ion and water adsorption at the surface, which are quite different on graphene and on hBN. Our work provides first principles insights into the structure and osmotic transport of aqueous electrolytes on two-dimensional materials and explores new pathways for efficient water desalination and osmotic energy conversion.

## Keywords

osmotic transport, blue energy, nanofluidics, electrical double layer, *ab initio* molecular dynamics, two-dimensional materials, graphene, hBN

## Introduction

Universal access to drinkable water and widespread production of electricity from renewable energy sources are two of the most daring challenges faced by modern society.

Progress in the field of nanofluidics offers alternative solutions to water desalination and to energy conversion through the mixing of salty and fresh water, so-called “blue” energy harvesting. Over the past decade, many novel osmotic transport phenomena have been observed in nanofluidic systems.<sup>1–4</sup> Among several noticeable examples is the osmotic current generated across boron nitride nanotubes and MoS<sub>2</sub> nanopores, whose power densities exceed by several orders of magnitude those produced by conventional membranes.<sup>5,6</sup> A further example is the observation of qualitatively different current-voltage characteristics in the nonlinear transport of ions across graphene and hBN angstrom-scale slits, which interestingly hints at the critical role of the crystal and electronic structure of the interface.<sup>7</sup> The measurement of conductance oscillations and Coulomb blockade in sub-nanometers MoS<sub>2</sub> pores also indicates that chemical nature, dimensions and geometry of nanopores are key factors to the observed nonlinear behaviours.<sup>8</sup> Thus, it stands to reason that obtaining a molecular-level picture of aqueous interfaces is essential to predict and control osmotic transport phenomena, and may lead to fundamental advances in the field of nanofluidics.

A comprehensive picture of the structure of water and electrolyte solutions at electrified surfaces, in the so-called electrical double layer (EDL), has not been obtained so far. Specifically, the structure of the EDL is not accurately described using the standard Gouy-Chapman theory of the EDL based on the Poisson-Boltzmann (PB) equation.<sup>9</sup> For instance, in a thin region of the EDL – typically of the order of 1 nm – ions may interact specifically with solid surfaces. Ion-specific effects in this region, which we define “adsorption layer”, are not captured by the standard PB equation.<sup>10,11</sup> Additionally, the PB theory of the EDL typically neglects the polar nature of water and water layering at the liquid/solid interface, and ignores spatial and dynamic interface heterogeneities.<sup>12–16</sup> Experimentally, a vast array of techniques have been used to probe the structure of the EDL.<sup>13</sup> Recent examples include second harmonic generation, which has revealed

structural and dynamical heterogeneities in the water orientation at the interface with silica,<sup>17</sup> and ambient pressure X-ray photoelectron spectroscopy, which has probed the shape of the electrostatic potential profile of aqueous electrolytes on gold electrodes at different concentrations.<sup>18</sup> Despite the tremendous advancement these types of work represent for the field, achieving sub-nanometer resolution, which is required to characterise the molecular structure of the EDL, remains an open experimental challenge.

A further challenge is to link the structure of aqueous interfaces to osmotic transport properties. Although experiments have hinted at the predominant role of charged groups, pore geometry and pore chemistry,<sup>13</sup> a microscopic characterization of the interface under operating conditions has not been obtained. Alternatively, atomistic simulations, and in particular molecular dynamics, can be used to explore the structure of the EDL at the molecular level. Force-field molecular dynamics (FFMD), which is based on an empirical description of the interactions between the constituent atoms, has yielded invaluable insights into the structure of the EDL<sup>19–22</sup> and into the molecular mechanisms underlying liquid and solute transport in nanofluidics<sup>11,23–35</sup> Yet, it is challenging to determine accurate force fields that incorporate electronic structure effects observed at complex liquid/solid interfaces. In contrast, *ab initio* molecular dynamics (AIMD) simulations based on density functional theory (DFT) are instrumental to compare the structure and dynamics of different aqueous interfaces on equal footing. Although AIMD is increasingly being used to characterise the structure of aqueous interfaces,<sup>36–40</sup> including OH<sup>−</sup> adsorption on two-dimensional materials,<sup>41</sup> H<sub>3</sub>O<sup>+</sup> adsorption on TiO<sub>2</sub><sup>42</sup> and ion adsorption at the liquid/vapour interface,<sup>43,44</sup> the impact of ion- and water-specific interactions on osmotic transport at aqueous interfaces has not been investigated with AIMD so far.

In this work we tackle two challenges: we determine the structure of model aqueous electrolyte interfaces from *ab initio* methods and we compute the mobilities underlying osmotic

transport processes due to different applied external fields (see Fig. 1). Our systems consist of a potassium iodide (KI) solution at the aqueous graphene and hBN interfaces. We chose the aqueous graphene and hBN interfaces because they are well-studied model systems in nanofluidics and for their potential impact as nano-osmotic power generators.<sup>4</sup> Also, we focus on KI as a model electrolyte displaying ion-specific effects.<sup>11,44,45</sup> The structure of the EDL and osmotic transport coefficients are computed according to the following steps: First, we calculate the free energy of adsorption of  $K^+$  and  $I^-$  ions dissolved in a 2 nanometer-thick water film using enhanced sampling techniques based on AIMD (a snapshot of a representative system is shown in the inset of Fig. 2(a)); Second, we obtain the electrostatic potential profile and the spatial distributions of the ions at different salt concentrations by solving a modified Poisson-Boltzmann (mPB) equation that accounts for the ions' free energy of adsorption on the sheets; Finally, osmotic transport coefficients are obtained, within linear response theory, by computing the relevant fluxes resulting from each external field, based on Stokes equation with a slip boundary condition at the wall. We find remarkable ion- and surface-specific adsorption of KI at the graphene and hBN interface. Such specific effects give rise to concentration-dependent scaling laws of the osmotic transport coefficients and result into strikingly different osmotic transport behaviour at the graphene and hBN interface. We rationalize the obtained scaling laws with a theoretical model that describes ion and water adsorption in terms of characteristic length-scales that are limited to a few molecular diameters.

## Results

### Unified framework of osmotic transport

One of the main objectives of this work is to provide a theoretical framework to calculate the osmotic transport coefficients from the molecular structure of water and ions at liquid/solid

interfaces. We do so within linear response theory, where the system of equations shown in Fig. 1 describes the thermodynamic fluxes resulting from applied external forces. The desired transport coefficients are the off-diagonal elements of the matrix shown in the middle of Fig. 1, and obey Onsager's reciprocal relations,<sup>46,47</sup> *i.e.* the matrix is symmetric. The osmotic transport coefficients are computed from hydrodynamics through the Stokes equation, in which the velocity profile is obtained using a partial slip boundary condition at the wall  $v(z=0) = b\partial_z v(z=0)$ , with  $b$  the slip length.<sup>48</sup> Throughout this work we thus assume that continuum hydrodynamics is valid at the nanoscale and that the viscosity is homogeneous. On hydrophobic, slipping surfaces such as the ones considered in this work, our assumptions have been shown to provide an accurate description of the velocity profiles even in the first molecular layers of the liquid.<sup>15</sup>

We start with electro-osmosis (EO), the flow generated by an electric field along a nanochannel, whose transport coefficient is illustrated in the top-right element of the matrix in Fig. 1. The electro-osmotic response is commonly quantified by the so-called zeta potential  $\zeta$ , which relates the electro-osmotic velocity in the bulk liquid  $v_{eo}$  to the electric field along the channel  $E$  through the Helmholtz-Smoluchowski relation:  $v_{eo} = -(\varepsilon\zeta/\eta)E$ , with  $\varepsilon$  and  $\eta$  the permittivity and viscosity of the liquid in bulk, respectively. According to Onsager's reciprocal relations,  $\zeta$  also quantifies the streaming current density  $j_e$  generated by a pressure gradient  $-\nabla p$  along the channel:  $j_e = -(\varepsilon\zeta/\eta)(-\nabla p)$ . From hydrodynamics equations, one can relate the  $\zeta$ -potential to the charge density profile at the interface (see *e.g.* Refs. 11,49 and the supporting information (SI)):

$$\zeta = -\frac{1}{\varepsilon} \int_0^\infty (z+b)\rho_e(z) dz, \quad (1)$$

where the charge density distribution is given by  $\rho_e = q_e(n_+ - n_-)$ , with  $n_+$  and  $n_-$  the cation and anion number densities, respectively, and  $q_e$  the elementary charge. Note that no

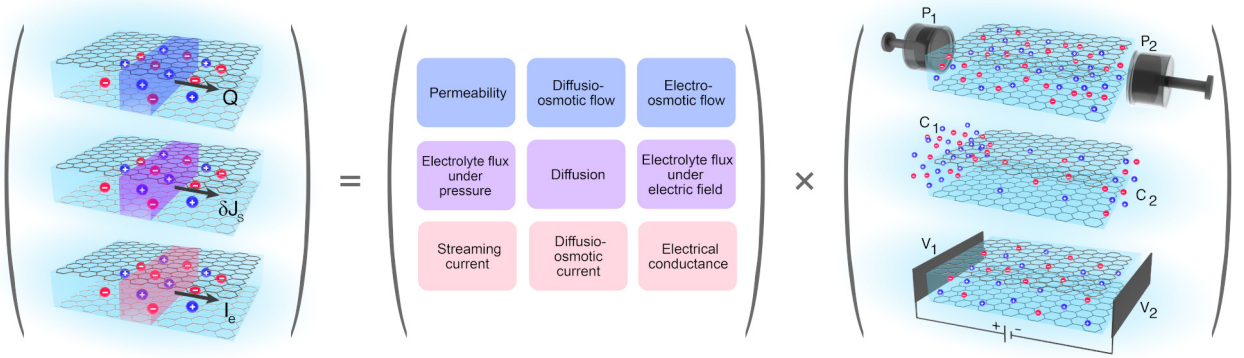


Figure 1: Schematic of the linear system of equations for osmotic transport. The off-diagonal elements of Onsager transport matrix represent the osmotic transport coefficients, and are the central quantities obtained in this work. They are computed from the linear response of the fluxes, (vector schematically shown on the left) to an applied external force (vector on the right). The matrix elements are color-coded according to the color labeling of the respective flux, i.e., blue, violet and pink for the elements due to a volumetric flow rate  $Q$ , an excess solute flux  $\delta J_s$  and an electrical current  $I_e$ , respectively. From top to bottom, the external force vector on the right labels a pressure gradient, a concentration gradient and an electrostatic potential gradient. The sheets schematically depict a slit geometry, with cations and anions shown in blue and red. Schematic inspired from Ref. 49.

assumption was made on the dielectric permittivity of the system: the bulk dielectric permittivity  $\epsilon$  only appears in Eq. (1) through the Helmholtz-Smoluchowski definition of  $\zeta$ .

We move on to introduce diffusio-osmosis (DO), the flow generated by a gradient of salt concentration along the channel<sup>50</sup> (see Fig. 1). Diffusio-osmosis can be quantified by the so-called diffusio-osmotic mobility  $D_{\text{DO}}$ , which relates the diffusio-osmotic velocity in the bulk liquid  $v_{\text{do}}$  to the gradient of salt concentration  $n_s$ :  $v_{\text{do}} = D_{\text{DO}}(-\nabla n_s/n_s)$ . Employing again Onsager's reciprocal relations,  $D_{\text{DO}}$  also quantifies the streaming excess solute flux density  $\delta j_s$  generated by a pressure gradient along the channel, see details in Ref. 29 and in the SI.

From hydrodynamics equations, one can relate  $D_{\text{DO}}$  to the ionic density profiles  $n_{\pm}(z)$  and to the water density profile  $n_w(z)$  (normalized by its bulk value  $n_w^b$ ) at the interface (see the

SI):

$$D_{\text{DO}} = \frac{k_B T}{\eta} \int_0^{\infty} (z+b) \times \left\{ n_+(z) + n_-(z) - 2n_s \frac{n_w(z)}{n_w^b} \right\} dz, \quad (2)$$

with  $k_B T$  the thermal energy. The integral expression for  $D_{\text{DO}}$  in Eq. (2) is a first central result of this work (see the derivation in the SI). In particular, the contribution of the water density profile, which is usually ignored in the theoretical expressions of  $D_{\text{DO}}$ ,<sup>49,51</sup> makes a key difference, as ignoring it leads to a spurious negative contribution to the integral in the vacuum-like region between the first water layer and the surface. Note that an additional flow can be generated under a salt concentration gradient: for salt ions with an asymmetric diffusivity, a so-called diffusion electric field  $E_0$  appears to avoid charge separation, creating an electro-osmotic flow, which adds to the intrinsic diffusio-osmotic flow.<sup>50,52</sup> However, as discussed in the SI (see Fig. S3), this electro-osmotic component is negligible in the systems considered here.

Finally, a gradient of salt concentration along the channel also generates an electric current, called diffusio-osmotic current (see Fig. 1), which is proportional to the perimeter of the channel cross section  $P$ . In order to quantify the intrinsic response of the liquid-solid interface, independently of the channel geometry, we therefore define the so-called diffusio-osmotic conductivity  $K_{\text{osm}}$ , which relates the diffusio-osmotic current generated per unit length of the channel circumference,  $I_e/P$ , to the gradient of salt concentration  $n_s$ :  $I_e/P = K_{\text{osm}}(-\nabla n_s/n_s)$ ; note that slightly different definitions can be found in the literature.<sup>5,49</sup> According to Onsager's reciprocal relations,  $K_{\text{osm}}$  also quantifies the excess solute flux generated by an electric field along the channel, see details in the SI. From hydrodynamics equations, and assuming a homogeneous dielectric permittivity (this assumption will be discussed later in the article), one can express  $K_{\text{osm}}$  as:

$$K_{\text{osm}} = \frac{k_B T q_e}{4\pi \ell_B \eta} \int_0^\infty \left[ \phi(z) - \phi_s - \frac{2 \operatorname{sgn}(\Sigma) b}{\ell_{\text{GC}}} \right] \times \left\{ n_+(z) + n_-(z) - 2n_s \frac{n_w(z)}{n_w^b} \right\} dz, \quad (3)$$

using the same notations as for Eq. (2), and with  $q_e$  the absolute ionic charge,  $\phi(z) = q_e V(z)/(k_B T)$  the reduced electrostatic potential,  $\phi_s$  its value at the surface,  $\ell_B = q_e^2/(4\pi\epsilon k_B T)$  the Bjerrum length (at which the electrostatic interaction between two ions is comparable to the thermal energy), and  $\ell_{\text{GC}} = q_e/(2\pi\ell_B|\Sigma|)$  the Gouy-Chapman length.<sup>53</sup> We remark that the expression for  $K_{\text{osm}}$  shown in Eq. (3) is the second important result of this work (see the SI for a complete derivation).

The ions' density and the electrostatic potential profiles appearing in Eqs. (1-3) are determined from the solution of the Poisson-Boltzmann equation,<sup>9,54</sup> which is used to describe the EDL near electrified interfaces and is modified to include the free energy of ion adsorption,<sup>10,45</sup> here computed from first princi-

ples simulations:

$$d_z^2 \phi(z) = -4\pi \ell_B [n_+(z) - n_-(z)] \\ = -4\pi \ell_B n_s [e^{-\phi(z)-g_+(z)} - e^{\phi(z)-g_-(z)}], \quad (4)$$

where the dimensionless free energies of ion adsorption  $g_\pm(z) = \Delta G_\pm(z)/(k_B T)$  are the key terms that distinguish Eq. (4) from the standard PB description of the EDL, and which importantly enable the possibility for non-zero solutions of Eq. (4) even in the absence of charged surfaces, as it is the case in our aqueous graphene and hBN interfaces. Although the form of Eq. (4) assumes a constant value of the dielectric permittivity  $\epsilon$ , we have also considered a step model of the dielectric constant<sup>11,45</sup> and we have computed the transport coefficients within this model in the SI (see Fig. S4). Whereas the electro-osmotic and diffusio-osmotic coefficients are not affected by the particular choice made for  $\epsilon$ , the magnitude of the diffusio-osmotic conductivity is altered depending on the model used for the dielectric constant; still, the scaling as a function of concentration and the change of sign remain the same, thus not affecting the conclusion of our work (see the SI).

## Ion adsorption and water density oscillations from first principles

Thus, we start to discuss our simulation results by presenting the free energy profiles of  $\text{I}^-$  and  $\text{K}^+$  and the water density profiles on graphene and hBN. Figs. 2(a) and (b) display the free energy of ion adsorption obtained from our *ab initio* umbrella sampling simulations. Significant ion- and surface-specific adsorption can be observed, which are limited to a region of about 1 nm from the sheets. Further, the free energy of adsorption of the  $\text{K}^+$  ion is essentially the same on graphene and hBN, and whilst the signature of a local minimum appears at a height of about 0.4 nm from the sheets,  $\text{K}^+$  is clearly more stable in the bulk water region. On the other hand, the free energy profile of  $\text{I}^-$  exhibits pronounced differences on graphene and hBN: a global minimum of about  $-0.08$

eV and  $-0.06$  eV is observed on graphene and hBN, respectively, where  $I^-$  is physisorbed at a height of about  $0.4$  nm on both sheets. Direct anion-substrate interactions due to van der Waals dispersion forces are likely responsible for the observed minimum, as reported in previous FFMD simulations and second harmonic generation experiments performed on closely related systems.<sup>55</sup> Interestingly, an energy barrier of about  $0.07$  eV is observed for  $I^-$  on hBN between the adsorption minimum at a height of  $0.4$  nm and the bulk water region at about  $1$  nm from the sheet. On graphene instead, a free energy barrier is not observed. Analysis of the dipole orientation of water at the two interfaces (reported in the SI in Fig. S2) suggests that subtle differences in the water dipole orientation on the two sheets may be responsible for the distinct features of the free energy profile of  $I^-$  on graphene and on hBN. While some changes in the water dipole orientations on the two sheets are noticed, the water spatial density distribution is remarkably similar on graphene and hBN and presents strong oscillations that are gradually suppressed above  $1.0$ - $1.2$  nm from the surface, as highlighted in previous work.<sup>56</sup> In Eq. (4), the ion density distributions, the electrostatic potential profile  $\phi(z)$  and its value at the sheets  $\phi_s$  depend non-linearly on the bulk salt concentration  $n_s$  through the free energy profiles shown in Fig. 2(a) and (b). Both the free energy profiles of the ions adsorbed on the sheets and the water density profile  $n_w(z)$  enter the transport integral expressions (Eqs. (1-3)) and are therefore key to understand osmotic transport at the interface.

## Concentration dependence of osmotic transport

The observed ion- and surface-specific adsorption and the layering of the water density profiles have pronounced effects on the osmotic transport coefficients. Slippage can also enhance osmotic transport dramatically,<sup>29</sup> as it can be evinced from Eqs. (1-3). In this work, we used slip length values taken from previous AIMD results.<sup>57</sup> Water flows significantly faster on graphene ( $b = 19.6$  nm) than on hBN

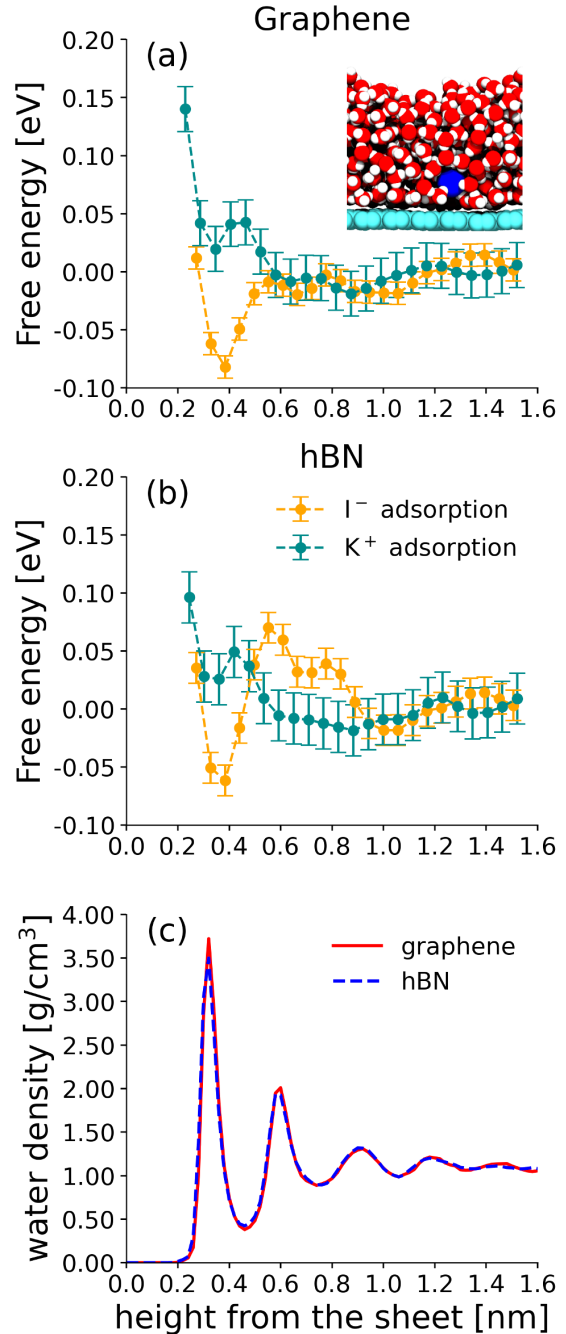


Figure 2: Free energy of  $I^-$  and  $K^+$  adsorption on (a) graphene and (b) hBN as a function of the height from the sheets, and (c) water density profile on graphene and hBN. The inset in (a) is a representative snapshot of the water film simulation with a iodide ion (blue) adsorbed on graphene (cyan). The free energy profile of  $K^+$  is similar on graphene and hBN and does not show an adsorption minimum, in contrast with  $I^-$  adsorption, which reveals a minimum near the sheets and a barrier on hBN, but not on graphene.

( $b = 4.0$  nm), and we wish to explore the consequences this bears for osmotic transport.

The osmotic transport coefficients are displayed in Fig. 3: Each transport coefficient follows a different asymptotic behaviour as a function of salt concentration and remarkable changes are noticed also between graphene and hBN. Fig. 3(a) is a schematic representation of electro-osmosis for the systems considered here, and Fig. 3(b) shows the absolute value of the  $\zeta$ -potential as a function of concentration. The absolute value of the  $\zeta$  potential increases from about 0.6 mV to 40 mV on graphene and from about 0.1 mV to 20 mV on hBN. A non-zero value of the  $\zeta$  potential even in absence of a surface charge highlights the role of ion-specific adsorption on electro-osmosis, as reported in the past by electro-phoretic experiments and FFMD simulations.<sup>11,58</sup> It is also worth noting that the slip contribution in Eq. (1) writes  $-b/\varepsilon \int_0^\infty dz \rho_e = b\Sigma/\varepsilon$ , so that it vanishes for neutral surfaces.<sup>11</sup> Thus, based on the form of Eq. (1), it can be evinced that both the magnitude and the different concentration dependence of  $\zeta$  on graphene and hBN solely arise from differences in the free energy profile of adsorption of  $I^-$  on the two sheets, given that the free energy of  $K^+$  is very similar on graphene and hBN.

A schematic representation of diffusio-osmotic flow is illustrated in Fig. 3(c) and the concentration dependence of the diffusio-osmotic coefficient  $D_{DO}$  is presented in Fig. 3(d). Whereas  $D_{DO}$  scales linearly on graphene at all concentrations, deviations from a linear asymptotics is noticed on hBN already around  $10^{-1}$  M, and above 1 M  $D_{DO}$  becomes negative (a positive value of  $D_{DO}$  indicates that the diffusio-osmotic flow proceeds from high to low concentration and vice-versa for negative  $D_{DO}$ ). Noting also that the  $K^+$  free energy profiles and the water spatial distribution are very similar on graphene and hBN, it is clear that  $D_{DO}$  changes sign on hBN because of the different free energy of adsorption of  $I^-$  from graphene. We note that a liquid flow that proceeds towards a larger concentration has been observed before for neutral solutes, which only interact specifically with

the surfaces.<sup>52,59</sup> Opposite to electro-osmotic transport, diffusio-osmotic transport is amplified by slippage even in the absence of a surface charge (see Eq. 2) and a strong slip-induced enhancement of the diffusio-osmotic flow has been reported before.<sup>29</sup> The larger slip-length, along with the absence of an adsorption barrier of  $I^-$  are the two main reasons why  $|D_{DO}|$  is larger on graphene than on hBN.

Finally, a schematic of the diffusio-osmotic current mechanism is presented in Fig. 3(e), and the scaling behaviour of the diffusio-osmotic conductivity is shown in Fig. 3(e). Below  $10^{-1}$  M, the diffusio-osmotic conductivity exhibits a different scaling behaviour with salt concentration on graphene and hBN, in contrast to what was observed in the case of the diffusio-osmotic coefficient. On graphene,  $K_{osm}$  scales more slowly than on hBN, but it remains positive at all concentrations considered. On hBN on the other hand, a maximum in  $K_{osm}$  is observed just below 1 M, above which an abrupt sign change is observed, similar to what observed for  $D_{DO}$ . Finally, in Eq. (3), we note that in contrast to  $D_{DO}$ , slippage does not contribute to  $K_{osm}$  in the absence of a surface charge, for which  $1/\ell_{GC} \propto \Sigma = 0$ . This is because slip shifts the DO velocity profile by a constant amount  $v_{slip}$ , so that the corresponding electrical current writes:  $I_e \propto v_{slip} \int_0^\infty dz \rho_e \propto v_{slip}(-\Sigma)$ , and vanishes for neutral surfaces.

## Scaling laws of the osmotic transport coefficients

To rationalize the different scaling properties, we introduce an effective surface charge (ESC) model of the EDL. The ESC model is discussed in full detail in the SI, but here we present the essential idea. In this model, the structure of the EDL is mapped to a standard PB description, where the effects associated to ion-specific adsorption are treated as surface terms by introducing an effective surface charge  $\Sigma_{eff}$ .  $\Sigma_{eff}$  is defined as  $\Sigma_{eff} = q_e n_s (e^{-\phi_s} K_+ - e^{\phi_s} K_-)$  and it depends on the bulk salt concentration  $n_s$ , on the surface potential  $\phi_s$  and on the characteristic lengths  $K_\pm$ , which quantify the excess or depletion of ions near the sheets (see

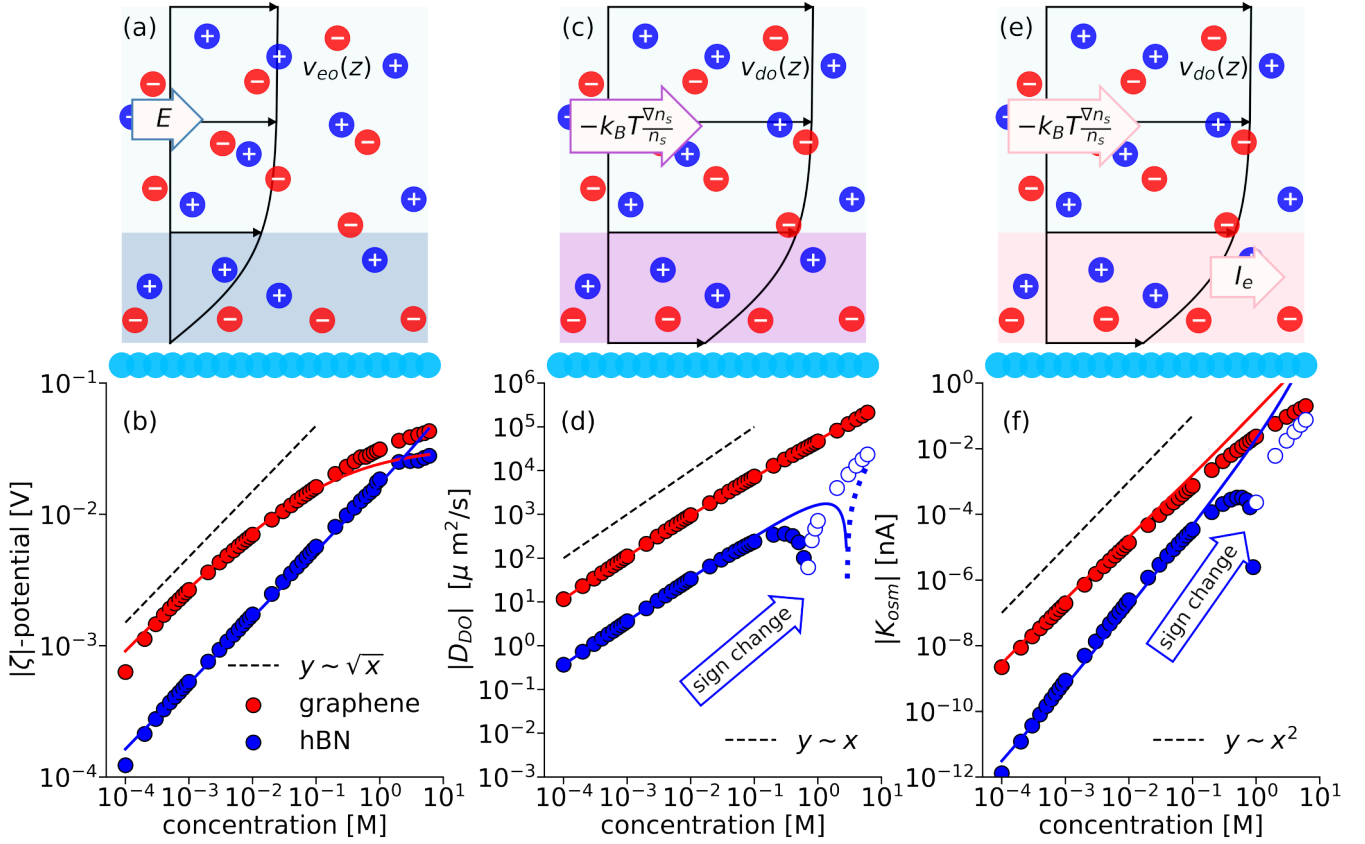


Figure 3: Molecular representation and concentration dependent scaling of osmotic transport at the aqueous graphene and hBN interfaces. Schematic of the electro-osmotic velocity profile  $v_{eo}(z)$  arising from an electric field  $E$  (a) and absolute value of the  $\zeta$  potential as a function of salt concentration (b); Schematic of the diffusio-osmotic velocity profile  $v_{do}(z)$  in response to a concentration gradient  $-k_B T(\nabla n_s)/n_s$  (c) and absolute value of the diffusio-osmotic coefficient  $|D_{DO}|$  (d); Representation of the diffusio-osmotic current  $I_e$  arising from a concentration gradient  $-k_B T(\nabla n_s)/n_s$  (e), and absolute value of the diffusio-osmotic conductivity  $|K_{osm}|$  (f). The transport coefficients display different scaling behaviours (see dashed lines). The symbols are obtained from the numerical integration of Eqs. (1-3), whereas the solid and dotted lines are from the effective surface charge model. In (d) and (f) the arrows point to a sign change, whereby  $D_{DO}$  and  $K_{osm}$  are negative on hBN at concentrations  $\gtrsim 1$  M, as indicated also by the empty symbols and dotted line in (d). In (a)  $v_{eo}(z)$  is not enhanced by slippage, opposite to  $v_{do}(z)$  in (c) and (e), see text for details.

the definition in Table 1). It will be shown that the density oscillations of interfacial water also enter this modified formulation and are relevant to capture diffusio-osmotic transport. The key to this simplified description is that the region where ions and water interact specifically with the sheets is very thin compared to the EDL. As such, the ESC model is strictly valid when there is a net separation between the water and ion adsorption length-scales and those of the EDL, given by the Debye length

and the effective Gouy-Chapman length, which we define here in terms of the effective surface charge  $\ell_{GC}^{eff} = q_e / (2\pi\ell_B|\Sigma_{eff}|)$ . In the following, we will apply the ESC model to Eqs. (1-3) to rationalize the scaling behaviours observed in Fig. 3.

Starting from electro-osmosis, the  $\zeta$ -potential can be expressed within the ESC model, in the limit of small reduced surface potentials  $\phi_s \ll 1$



(see the SI), as:

$$\zeta \approx \frac{k_B T}{q_e} \phi_s \approx \frac{k_B T}{q_e} \cdot \frac{K_+ - K_-}{2\lambda_D + K_+ + K_-}. \quad (5)$$

The results of this equation are shown as solid lines in Fig. 3(b). To understand the two different limits observed in the figure, it is instrumental to inspect the values of the ion-specific length-scales  $K_+$  and  $K_-$  entering the equation, which are listed in Table 1. For both graphene and hBN,  $K_+$  is negative and indicates a net depletion of cations near the sheets, whereas  $K_-$  is positive and indicates a net accumulation of anions. Noting also that for hBN,  $|K_+ + K_-| \ll \lambda_D$  at all concentrations, Eq. (5) simplifies to  $\zeta \approx k_B T (K_+ - K_-) / (2\lambda_D q_e)$ , such that  $\zeta$  scales as the inverse of the Debye length, or equivalently as the square-root of the salt concentration, *i.e.*,  $\zeta \sim 1/\lambda_D \sim \sqrt{n_s}$ . For graphene on the other hand, departure from  $\zeta \sim \sqrt{n_s}$  is visible already at a concentration above  $10^{-3}$  M because the term  $|K_+ + K_-|$  becomes comparable to  $\lambda_D$ . Therefore, approximately above  $10^{-3}$  M the scaling of  $\zeta$  on graphene is better captured by the full Eq. (5). Beyond  $10^{-1}$  M for graphene and beyond 1 M for hBN, the prediction from Eq. (5) deviates from the numerically integrated results because the surface potential becomes of the order of the thermal voltage (*i.e.*  $\phi_s \gtrsim 1$ ).

Application of the ESC model to diffusio-osmosis (Eq. (2)) yields the following relation for  $D_{DO}$  (derived in the SI):

$$D_{DO} \approx \frac{k_B T}{2\pi\ell_B\eta} \left\{ -\ln(1 - \gamma^2) + \frac{b|\gamma|}{\ell_{GC}^{\text{eff}}} + \frac{1}{4\lambda_D^2} [e^{-\phi_s} K_+ L_+ + e^{\phi_s} K_- L_- - 2K_w L_w + b(e^{-\phi_s} K_+ + e^{\phi_s} K_- - 2K_w)] \right\}. \quad (6)$$

The first two terms depending on  $\gamma$ , with  $\gamma = \tanh(\phi_s/4)$ , result from a calculation of the diffusio-osmotic flow according to the standard PB description of the EDL<sup>50,51</sup> and arise from the region in the EDL beyond the adsorption layer, whereas the remaining terms involving the ion length-scales ( $K_{\pm}$  and  $L_{\pm}$ )

and the water length-scales ( $K_w$  and  $L_w$ ) arise from specific interactions within the adsorption layer. Along with  $K_{\pm}$ , the additional ion-specific length-scales  $L_{\pm}$  contributing to Eq. (6) (see definition in Table 1) represent the characteristic thicknesses over which cations and anions adsorb. The water-specific length-scale  $K_w$  is characteristic of a net accumulation or depletion of water near the sheets, while  $L_w$  represents the characteristic size over which water accumulates/depletes at the aqueous interface (see definition in Table 1). By analysing the relevant terms in Eq. (6), we can interpret the scaling behaviour observed in Fig. 3(c), while pointing out that in the equation  $\lambda_D$ ,  $\ell_{GC}^{\text{eff}}$ ,  $\gamma$  and  $\phi_s$  all depend on concentration. First, the terms depending on  $\gamma$  are negligible compared to the adsorption layer terms at small surface potentials ( $\phi_s < 1$ ) and at concentrations below  $\sim 10^{-1}$  M because to leading order  $\gamma \sim \phi_s$  whereas  $e^{\pm\phi_s} \sim 1$ . Therefore, at low concentrations a linear dependence of  $D_{DO}$  can be readily understood based on the dependence of the adsorption term proportional to  $\lambda_D^{-2}$  by realizing that  $D_{DO} \sim \lambda_D^{-2} \sim n_s$ . Also, examining the characteristic length-scales listed in Table 1, one notices that the terms involving  $e^{\mp\phi_s} K_{\pm} L_{\pm}$  and  $2K_w L_w$  can be neglected compared to the factor proportional to  $b$  because the slip length is much larger than  $|L_{\pm}|$  and  $|L_w|$ . As such,  $D_{DO}$  is enhanced by slippage through the slip length  $b$  and the magnitude of  $D_{DO}$  is larger on graphene than on hBN partly because of the larger slip length in the former material. As the concentration is increased around 1 M the PB term and in particular the slip contribution  $b|\gamma|/\ell_{GC}^{\text{eff}}$  can no longer be neglected. Interestingly, competing effects between the  $b|\gamma|/\ell_{GC}^{\text{eff}}$  term, the ions' adsorption term and the molecular-scale oscillations of water can give rise to a sign reversal in  $D_{DO}$  at a critical concentration. Reversal of diffusio-osmotic flow is indeed observed on hBN, but not on graphene, due to the differences in the slip length and in the ion adsorption length-scales between the two materials (see Table 1). On graphene, the ion-specific adsorption terms proportional to  $e^{-\phi_s} K_+ + e^{\phi_s} K_-$  and the term proportional to  $b|\gamma|/\ell_{GC}^{\text{eff}}$  dominate over the wa-

Table 1: Slip length ( $b$ ) and length-scales characteristic of cation-specific (with subscripts “+”), anion-specific adsorption (with subscripts “−”) and water density oscillations (with subscript “ $w$ ”) at the aqueous graphene and hBN interfaces, along with their definitions. The slip length and the anion length-scales are in bold to highlight the stark differences between graphene and hBN.

lengths [nm]	definition	graphene	hBN
<b><math>b</math></b>		<b>+19.6</b>	<b>+4.0</b>
$K_+$	$\int_0^\infty [e^{-g_+(z)} - 1] dz$	−0.229	−0.207
<b><math>K_-</math></b>	$\int_0^\infty [e^{-g_-(z)} - 1] dz$	<b>+1.974</b>	<b>+0.177</b>
$K_w$	$\int_0^\infty [n_w(z)/n_w^b - 1] dz$	−0.179	−0.165
$L_+$	$K_+^{-1} \int_0^\infty z [e^{-g_+(z)} - 1] dz$	−0.363	−0.442
<b><math>L_-</math></b>	$K_-^{-1} \int_0^\infty z [e^{-g_-(z)} - 1] dz$	<b>+0.459</b>	<b>−0.099</b>
$L_w$	$K_w^{-1} \int_0^\infty z [n_w(z)/n_w^b - 1] dz$	−0.031	−0.027

ter contribution proportional to  $2K_w$  at all concentrations and the diffusio-osmotic flow always proceeds in the direction from high to low concentrations. On hBN, instead, above a critical concentration of about 1 M the water term becomes the dominant contribution and a flow reversal is observed. A more detailed analysis on the scaling behaviour of  $D_{DO}$  is provided in Fig. S5 in the SI, where the diffusio-osmotic coefficient has been explicitly decomposed into the standard PB contribution and the adsorption layer contribution.

Finally, an approximate expression for the diffusio-osmotic conductivity  $K_{\text{osm}}$  is obtained to understand the scaling behaviour observed in Fig. 3(c) as:

$$K_{\text{osm}} \approx -\frac{k_B T \Sigma_{\text{eff}}}{2\pi \ell_B \eta} \times \left( 1 - \frac{\text{asinh}(\chi)}{\chi} + \frac{e^{-\phi_s} \tilde{K}_+ \tilde{L}_+ + e^{\phi_s} \tilde{K}_- \tilde{L}_- - 2\tilde{K}_w \tilde{L}_w}{4\lambda_D^2} \right). \quad (7)$$

The term  $1 - \text{asinh}(\chi)/\chi$  arises from the region in the EDL beyond the adsorption layer, with  $\chi = \lambda_D/\ell_{\text{GC}}^{\text{eff}}$ .<sup>5,51</sup> The adsorption layer also contributes to  $K_{\text{osm}}$  through the ion-specific length-scales  $\tilde{K}_\pm$  and  $\tilde{L}_\pm$ , as well as  $\tilde{K}_w$  and  $\tilde{L}_w$ . Their interpretation is analogous to the characteristic lengths reported in Table 1, but we refer the reader to the SI (Table S1) for their definition and numerical values.

At concentrations between  $10^{-4}$  M and  $10^{-1}$  M, Eq. (7) reproduces the asymptotic behaviour of the diffusio-osmotic conductivity, which scales as  $K_{\text{osm}} \sim n_s^p$ , where  $p \approx 2$  for graphene and  $p \approx 2.5$  for hBN. We discuss each term separately to explain the scaling behaviour observed in Fig. 3(f). First of all, to leading order, the effective surface charge scales linearly with the salt concentration (*i.e.*,  $\Sigma_{\text{eff}} \sim n_s$ ). Secondly, noting that  $\ell_{\text{GC}}^{\text{eff}} \propto \Sigma_{\text{eff}}^{-1}$ , the contribution to the diffusio-osmotic conductivity arising from the region beyond the adsorption layer also scales linearly with salt concentration (*i.e.*,  $1 - \text{asinh}(\chi)/\chi \sim n_s$ ). Thirdly, the term arising from the adsorption layer exhibits a first obvious linear dependence on the concentration through the Debye length since  $\lambda_D^{-2} \propto n_s$ . This is indeed observed for graphene, such that overall the diffusio-osmotic conductivity scales as  $K_{\text{osm}} \sim n_s^2$ . A second more subtle dependence on salt concentration however, is observed on hBN, where the adsorption layer term in Eq. (7) changes sign around  $5 \times 10^{-3}$  M (see Fig. S6 in the SI). The contribution to the diffusio-osmotic conductivity coming from the adsorption layer term and the  $1 - \text{asinh}(\chi)/\chi$  term can be either suppressed or enhanced depending on the sign of the former, and ultimately results into a scaling of  $K_{\text{osm}} \sim n_s^{2.5}$ . Further, similarly to what was observed in the case of the diffusio-osmotic flow in Fig. 3(d), at concentrations

beyond 1 M a reversal in the diffusio-osmotic current is observed in the numerical calculations for hBN, because the water contribution dominates over its ion counterpart, whereas on graphene a sign change is not observed because the ion-specific adsorption contribution dominates at all considered concentrations. We note that the assumption of a linear electrostatic potential difference  $\phi(z) - \phi_s$  made while deriving Eq. (7) breaks down at large concentrations, thus Eq. (7) fails to predict the sign change on hBN at around 1 M.

## Discussion

In this section, we discuss the significance of our work in connection with theoretical and experimental results on the structure of the EDL and of osmotic transport in nanofluidics. In our approach to calculate the spatial distribution of ions in the EDL, the electrostatic potential and the free energy profile of ion adsorption are determined, respectively, from the solution of the mPB equation and from our enhanced sampling simulations. This framework has been introduced in the past to study the structure of the EDL at liquid/liquid interfaces<sup>10</sup> and to shed light on the Hofmeister series at hydrophobic and hydrophilic surfaces for different surface charges with FFMD simulations.<sup>45</sup> However, deviations from a modified PB description of the electrostatic potential appear at concentrations of the order of 1 M,<sup>12</sup> and it would be interesting to incorporate more advanced theories into our framework to ameliorate the deficiencies underlying the mPB theory at such concentrations.<sup>43,60–62</sup>

Despite their substantial computational cost, our *ab initio* simulations have also revealed that ion adsorption can be surface-specific, as illustrated by the differences in the free energy of  $I^-$  on the two sheets but not of  $K^+$ . In particular, the presence of a free energy barrier of  $I^-$  on hBN and not on graphene can be ascribed to differences in the water dipole orientation on the two sheets. Deep UV second harmonic generation, already used to investigate the free energy of adsorption of  $SCN^-$  on

graphene,<sup>55</sup> is an ideal technique to explore ion adsorption on other substrates, including hBN. Also, X-ray photoelectron spectroscopy would be instrumental to probe the shape of the electrostatic potential profile at aqueous electrified interfaces.<sup>18</sup>

A central contribution of this paper is to have provided a unified framework of osmotic transport that can be computed from the structure of water and ions at aqueous interfaces, and which transport coefficients can be probed experimentally. Measurements of osmotic transport of KI solutions across graphene or hBN have not appeared yet, but we think that they are already possible, given that measurements of ion transport across Å-size slits have been reported, and that diffusio-osmosis of several types of salts across silica surfaces has also been probed. It would be desirable that such experiments be performed at the point of zero charge, since differences in pH lead to variations in the surface charge<sup>5,51,63,64</sup> and thus would likely alter the scaling behaviour of the transport coefficients with concentration. For instance, a different scaling behaviour of the electrical conductivity on salt concentration has been observed in carbon nanotubes. This has been captured by charge regulation models<sup>63,65</sup> which are, however, phenomenologically different from the mechanisms described here, as we remark that the sheets are not charged.

In absence of experiments on KI solutions, we can connect our work to recent streaming-voltage experiments of KCl solutions across graphitic Å-size slits.<sup>66</sup> Such experiments did not present a clear dependence of the  $\zeta$ -potential as a function of concentration in a range between  $10^{-3}$  M and  $10^{-1}$  M and extracted a value for  $\zeta$  at least 10 times larger than that shown in Fig.3 (a). Possible explanations are that, although ion-specific effects of a KCl solution are less pronounced than a KI solution, under the extreme confinement regime probed in such experiments the Stokes equation of hydrodynamics breaks down. Additionally, ion exclusion at the entrance of the membranes might play an important role in Å-scale slits.

Concerning diffusio-osmosis, we discuss our results in connection with measurements per-

formed on silica surfaces, where the diffusio-osmotic coefficient has been measured for several types of aqueous electrolytes, including KI.<sup>52</sup> The reported diffusio-osmotic coefficient of KI on silica is  $D_{\text{DO}} \approx 250 \mu\text{m}^2/\text{s}$ , independent of concentration. Instead, we observe approximately a linear dependence at all concentrations for graphene, and above  $10^{-1} \text{ M}$   $D_{\text{DO}}$  reaches values beyond  $10^4 \mu\text{m}^2/\text{s}$ . The observed enhancement of the diffusio-osmotic flow of KI on graphene compared to silica can be largely attributed to the larger slip length of graphene. Although the *ab initio* values for the slip length on graphene and hBN<sup>57</sup> compare well to recent flow experiments performed on graphene slits,<sup>28</sup> as well as on hBN nanotubes and on carbon nanotubes with a large radius  $R$  of 50 nm,<sup>67</sup> the slip length for carbon nanotubes with a smaller radius  $R = 20 \text{ nm}$  is about one order of magnitude larger than that of graphene,  $b \sim 200 \text{ nm}$ . Provided that the structure of the EDL would be only modestly affected by such a large nanotube radius, one can extrapolate the value of the diffusio-osmotic coefficient that would be obtained for carbon nanotubes with  $R = 20 \text{ nm}$  from our results on graphene. Doing so would result in approximately a 10-fold enhancement in the diffusio-osmotic coefficient because of the much larger slip length. Additionally, compared to silica, where the diffusio-osmotic flow proceeds from high to low concentrations, we observe a flow reversal on hBN.

Measurements of the diffusio-osmotic current of KI solutions on graphene or hBN have also not been reported. As such, we connect our results for  $K_{\text{osm}}$  to osmotic energy conversion experiments of KCl solutions flowing across single-pore BN nanotubes.<sup>5</sup> On BN nanotubes, the diffusio-osmotic conductivity  $K_{\text{osm}}^{\text{BNNT}}$  has been extracted from the ratio between the diffusio-osmotic current and the difference in the salt concentration at the reservoirs as  $K_{\text{osm}}^{\text{BNNT}} = I_{\text{osm}}/(\Delta n_s/n_s)$ . In order to compare directly to our results, we normalize the current with respect to the perimeter  $P = 2\pi R$  and the length  $L$  of the nanotube, *i.e.*  $K_{\text{osm}}^{\text{BNNT}} = \frac{I_{\text{osm}}/P}{\Delta n_s/(n_s L)}$ . With an experimental value of the nanotube length  $L = 1250 \text{ nm}$  and of the radius  $R = 40 \text{ nm}$ , the equivalent exper-

imental value for the diffusio-osmotic conductivity is  $K_{\text{osm}}^{\text{BNNT}} = K_{\text{osm}}^{\text{BNNT}} L/(2\pi R) = 0.35 - 0.80 \text{ nA}$ . These values for the diffusio-osmotic conductivity are much larger than those computed here (at any salt concentration) because of the very large surface charge  $\Sigma$  that was reported in experiments ( $\Sigma \approx 0.1 - 1 \text{ C/m}^2$ ). In BN nanotubes, the diffusio-osmotic conductivity has been found to scale linearly on the pH of the solution, and thus on the surface charge, but to be independent of salt concentration.<sup>5</sup> Here instead, the diffusio-osmotic conductivity scales roughly as  $K_{\text{osm}} \sim n_s^p$  with an exponent  $p \approx 2$  and  $p \approx 2.5$  for graphene and hBN, respectively, over several decades of salt concentration. The sign reversal in the diffusio-osmotic current, as well as in the diffusio-osmotic flux, could be particularly relevant in biology. Similar mechanisms might be at work in membrane proteins, which could exploit changes in concentration to regulate charge and solute transport.<sup>68,69</sup> Although the focus here has been devoted to the understanding of osmotic transport across a single-pore membrane or channel, further challenges lie ahead of diffusio-osmosis in order to establish itself as a viable source of renewable energy, in particular, for what concerns the generation of electricity using multipore systems.<sup>3,4,70</sup>

In conclusion, we have provided a unified description of osmotic transport by coupling first principles simulations with a mean field description of the EDL and with the Stokes equation of hydrodynamics, and have applied this framework to understand the osmotic transport properties of a prototypical salt that displays pronounced ion-specific effects on two-dimensional materials. Through the mPB equation of the EDL (see Eq. (4)), the transport coefficients in Eqs. (1-3) can be readily computed from the spatial distribution of ions and water at the interface. We have reported on a concentration-dependent scaling behaviour of the osmotic transport coefficients at the aqueous graphene and hBN interfaces and explained it with a model that accounts for ion-specific adsorption and water layering in a thin region of the EDL of the order of 1 nm. The observed scaling, along with the possibility of diffusio-osmotic

flow and current reversal, may provide additional routes to further improve osmotic energy conversion. Moreover, it could foster the development of nanofluidic diodes and sensors and may be instrumental to shed light on the mechanisms underlying charge and solute transport across membrane proteins.

## Materials and Methods

### Electronic structure and *ab initio* molecular dynamics

The *ab initio* umbrella sampling simulations are performed with the CP2K code,<sup>71</sup> and the electronic structure problem is solved using DFT with the optB88-vdW functional.<sup>72,73</sup> The optB88-vdW functional has been applied to investigate slippage on two-dimensional materials<sup>57,74</sup> and it describes the structure of graphite and bulk hBN accurately.<sup>75</sup> Despite the limitations of most density functionals in describing water, the optB88-vdW functional appears to be one of the most satisfactory.<sup>76</sup> Reference quantum monte carlo calculations of water monomers adsorbed on graphene and hBN sheets<sup>77,78</sup> also show that this functional captures the relative stability of water on different adsorption sites.

The free energy of adsorption of  $K^+$  and  $I^-$  ions and the spatial water distribution were calculated from umbrella sampling simulations.<sup>79</sup> The systems consist of water films containing 400 molecules and approximately 2 nm-thick placed above a  $2.56 \times 2.46$  nm<sup>2</sup> graphene and a  $2.61 \times 2.51$  hBN nm<sup>2</sup> sheet. Separate umbrella sampling simulations were performed for potassium and iodide adsorption by restraining each ion at different heights  $z_0$  above the sheets with a harmonic bias potential  $U_b(z, t) = k_b/2(z(t) - z_0)^2$ ,  $z(t)$  being the instantaneous height of the ion above the sheets, and  $k_b = 836.8$  kJ/mol/nm<sup>2</sup> the *spring* constant. A total of 23 umbrella sampling windows were used for each system and for each window the dynamics were propagated for 40 ps in the NVT ensemble at 300 K within the Born-Oppenheimer approximation,

except for  $I^-$  adsorption on graphene, for which dynamics were propagated for additional 30 ps to test a possible dependence of our results on the length of the simulations. The free energy was reconstructed using umbrella integration.<sup>80</sup> Further computational details on the optimization of the wave-function and on the umbrella sampling simulations are reported in the SI. The tools used to perform the analysis and the CP2K input files to reproduce the main results of the manuscript have been deposited on GitHub and are available at [https://github.com/gabriele16/osmotic\\_transport\\_scaling\\_laws](https://github.com/gabriele16/osmotic_transport_scaling_laws).

**Acknowledgement** GT is supported by the SNSF project PZ00P2.179964. LJ is supported by the Institut Universitaire de France. RM and GT acknowledge funding by the Deutsche Forschungsgemeinschaft (DFG, German Research Foundation) – 390794421. We also thank the Swiss National Supercomputer Centre (CSCS) under PRACE for awarding us access to Piz Daint, Switzerland, through projects pr66 and s826.

## Supporting Information Available

Further computational details and tests on the structure and dynamics of water at the interface with graphene and hBN from force field and *ab initio* simulations; derivation of integral expressions for the transport coefficients; details of the modified Poisson-Boltzmann description; details of the effective surface charge model.

## References

1. Siria, A.; Bocquet, M.-L.; Bocquet, L. New avenues for the large-scale harvesting of blue energy. *Nature Reviews Chemistry* **2017**, *1*, 0091.
2. Wang, L.; Boutilier, M. S.; Kidambi, P. R.; Jang, D.; Hadjiconstantinou, N. G.; Karnik, R. Fundamental transport mechanisms, fabrication and potential applica-

- tions of nanoporous atomically thin membranes. *Nature Nanotechnology* **2017**, *12*, 509–522.
3. Tong, X.; Liu, S.; Crittenden, J.; Chen, Y. Nanofluidic Membranes to Address the Challenges of Salinity Gradient Power Harvesting. *ACS Nano* **2021**, *15*, 5838–5860.
  4. Macha, M.; Marion, S.; Nandigana, V. V. R.; Radenovic, A. 2D materials as an emerging platform for nanopore-based power generation. *Nature Reviews Materials* **2019**, *1*.
  5. Siria, A.; Poncharal, P.; Bianco, A.-L.; Fulcrand, R.; Blase, X.; Purcell, S. T.; Bocquet, L. Giant osmotic energy conversion measured in a single transmembrane boron nitride nanotube. *Nature* **2013**, *494*, 455–458.
  6. Feng, J.; Graf, M.; Liu, K.; Ovchinnikov, D.; Dumcenco, D.; Heiranian, M.; Nandigana, V.; Aluru, N. R.; Kis, A.; Radenovic, A. Single-layer MoS<sub>2</sub> nanopores as nanopower generators. *Nature* **2016**, *536*, 197–200.
  7. Esfandiari, A.; Radha, B.; Wang, F.; Yang, Q.; Hu, S.; Garaj, S.; Nair, R.; Geim, A.; Gopinadhan, K. Size effect in ion transport through Ångstrom-scale slits. *Science* **2017**, *358*, 511–513.
  8. Feng, J.; Liu, K.; Graf, M.; Dumcenco, D.; Kis, A.; Di Ventra, M.; Radenovic, A. Observation of ionic Coulomb blockade in nanopores. *Nature Materials* **2016**, *15*, 850–855.
  9. Hunter, R. J. *Foundations of colloid science*; Oxford University Press, 2001.
  10. Luo, G.; Malkova, S.; Yoon, J.; Schultz, D. G.; Lin, B.; Meron, M.; Benjamin, I.; Vanýsek, P.; Schlossman, M. L. Ion distributions near a liquid-liquid interface. *Science* **2006**, *311*, 216–218.
  11. Huang, D. M.; Cottin-Bizonne, C.; Ybert, C.; Bocquet, L. Ion-specific anomalous electrokinetic effects in hydrophobic nanochannels. *Physical Review Letters* **2007**, *98*, 177801.
  12. Gonella, G.; Backus, E. H.; Nagata, Y.; Bonthuis, D. J.; Loche, P.; Schlaich, A.; Netz, R. R.; Kühnle, A.; McCrum, I. T.; Koper, M. T., *et al.* Water at charged interfaces. *Nature Reviews Chemistry* **2021**, 1–20.
  13. Hartkamp, R.; Bianco, A.-L.; Fu, L.; Dufrière, J.-F.; Bonhomme, O.; Joly, L. Measuring surface charge: Why experimental characterization and molecular modeling should be coupled. *Current Opinion in Colloid & Interface Science* **2018**, *37*, 101–114.
  14. Markovich, T.; Andelman, D.; Orland, H. Ionic profiles close to dielectric discontinuities: Specific ion-surface interactions. *Journal of Chemical Physics* **2016**, *145*.
  15. Bonthuis, D. J.; Netz, R. R. Beyond the Continuum: How Molecular Solvent Structure Affects Electrostatics and Hydrodynamics at Solid–Electrolyte Interfaces. *The Journal of Physical Chemistry B* **2013**, *117*, 11397–11413.
  16. Limmer, D. T.; Willard, A. P.; Madden, P.; Chandler, D. Hydration of metal surfaces can be dynamically heterogeneous and hydrophobic. *Proceedings of the National Academy of Sciences* **2013**, *110*, 4200–4205.
  17. Macias-Romero, C.; Nahalka, I.; Okur, H. I.; Roke, S. Optical imaging of surface chemistry and dynamics in confinement. *Science* **2017**, *357*, 784–788.
  18. Favaro, M.; Jeong, B.; Ross, P. N.; Yano, J.; Hussain, Z.; Liu, Z.; Crumlin, E. J. Unravelling the electrochemical double layer by direct probing of the solid/liquid interface. *Nature Communications* **2016**, *7*, 1–8.

19. Siepmann, J. I.; Sprik, M. Influence of surface topology and electrostatic potential on water/electrode systems. *The Journal of Chemical Physics* **1995**, *102*, 511–524.
20. Scalfi, L.; Limmer, D. T.; Coretti, A.; Bonella, S.; Madden, P. A.; Salanne, M.; Rotenberg, B. Charge fluctuations from molecular simulations in the constant-potential ensemble. *Physical Chemistry Chemical Physics* **2020**,
21. Scalfi, L.; Dufils, T.; Reeves, K. G.; Rotenberg, B.; Salanne, M. A semiclassical Thomas-Fermi model to tune the metallicity of electrodes in molecular simulations. *The Journal of Chemical Physics* **2020**, *153*.
22. Limmer, D. T.; Merlet, C.; Salanne, M.; Chandler, D.; Madden, P. A.; Van Roij, R.; Rotenberg, B. Charge fluctuations in nanoscale capacitors. *Physical Review Letters* **2013**, *111*, 1–5.
23. Striolo, A.; Michaelides, A.; Joly, L. The Carbon-Water Interface: Modeling Challenges and Opportunities for the Water-Energy Nexus. *Annual Review of Chemical and Biomolecular Engineering* **2016**, *7*, 533–556.
24. Phan, A.; Cole, D. R.; Weiß, R. G.; Dzubiella, J.; Striolo, A. Confined water determines transport properties of guest molecules in narrow pores. *ACS Nano* **2016**, *10*, 7646–7656.
25. Faucher, S.; Aluru, N.; Bazant, M. Z.; Blankschtein, D.; Brozena, A. H.; Cummings, J.; Pedro de Souza, J.; Elimelech, M.; Epsztein, R.; Fourkas, J. T.; Rajan, A. G.; Kulik, H. J.; Levy, A.; Majumdar, A.; Martin, C.; McEldrew, M.; Misra, R. P.; Noy, A.; Pham, T. A.; Reed, M.; Schweigler, E.; Siwy, Z.; Wang, Y.; Strano, M. Critical Knowledge Gaps in Mass Transport through Single-Digit Nanopores: A Review and Perspective. *The Journal of Physical Chemistry C* **2019**, *123*, 21309–21326.
26. Falk, K.; Sedlmeier, F.; Joly, L.; Netz, R. R.; Bocquet, L. Molecular origin of fast water transport in carbon nanotube membranes: Superlubricity versus curvature dependent friction. *Nano Letters* **2010**, *10*, 4067–4073.
27. Ma, M.; Grey, F.; Shen, L.; Urbakh, M.; Wu, S.; Liu, J. Z.; Liu, Y.; Zheng, Q. Water transport inside carbon nanotubes mediated by phonon-induced oscillating friction. *Nature Nanotechnology* **2015**, *10*, 692–695.
28. Xie, Q.; Alibakhshi, M. A.; Jiao, S.; Xu, Z.; Hempel, M.; Kong, J.; Park, H. G.; Duan, C. Fast water transport in graphene nanofluidic channels. *Nature Nanotechnology* **2018**, *13*, 238.
29. Ajdari, A.; Bocquet, L. Giant Amplification of Interfacially Driven Transport by Hydrodynamic Slip: Diffusio-Osmosis and Beyond. *Physical Review Letters* **2006**, *96*, 186102.
30. Heiranian, M.; Farimani, A. B.; Aluru, N. R. Water desalination with a single-layer MoS<sub>2</sub> nanopore. *Nature Communications* **2015**, *6*, 1–6.
31. Noh, Y.; Aluru, N. R. Ion Transport in Electrically Imperfect Nanopores. *ACS Nano* **2020**, *14*, 10518–10526.
32. Liu, Y.; Ganti, R.; Frenkel, D. Pressure gradients fail to predict diffusio-osmosis. *Journal of Physics: Condensed Matter* **2018**, *30*, 205002.
33. Simoncelli, M.; Ganfoud, N.; Sene, A.; Haefele, M.; Daffos, B.; Taberna, P.-L.; Salanne, M.; Simon, P.; Rotenberg, B. Blue energy and desalination with nanoporous carbon electrodes: Capacitance from molecular simulations to continuous models. *Physical Review X* **2018**, *8*, 021024.
34. Kalra, A.; Garde, S.; Hummer, G. Osmotic water transport through carbon nanotube membranes. *Proceedings of the National*

- Academy of Sciences* **2003**, *100*, 10175–10180.
35. Zhou, K.-G.; Vasu, K. S.; Cherian, C. T.; Neek-Amal, M.; Zhang, J. C.; Ghorbanfekr-Kalashami, H.; Huang, K.; Marshall, O. P.; Kravets, V. G.; Abraham, J.; Su, Y.; Grigorenko, A. N.; Pratt, A.; Geim, A. K.; Peeters, F. M.; Novoselov, K. S.; Nair, R. R. Electrically controlled water permeation through graphene oxide membranes. *Nature* **2018**, *559*, 236–240.
  36. Le, J.-B.; Fan, Q.-Y.; Li, J.-Q.; Cheng, J. Molecular origin of negative component of Helmholtz capacitance at electrified Pt (111)/water interface. *Science Advances* **2020**, *6*, eabb1219.
  37. Cheng, J.; Sprik, M. Alignment of electronic energy levels at electrochemical interfaces. *Physical Chemistry Chemical Physics* **2012**, *14*, 11245–11267.
  38. Groß, A.; Sakong, S. Modelling the electric double layer at electrode/electrolyte interfaces. *Current Opinion in Electrochemistry* **2019**, *14*, 1–6.
  39. Lan, J.; Rybkin, V. V.; Iannuzzi, M. Ionization of water as an effect of quantum delocalization at aqueous electrode interfaces. *The Journal of Physical Chemistry Letters* **2020**, *11*, 3724–3730.
  40. Seiler, S.; Halbig, C. E.; Grote, F.; Rietsch, P.; Börrnert, F.; Kaiser, U.; Meyer, B.; Eigler, S. Effect of friction on oxidative graphite intercalation and high-quality graphene formation. *Nature Communications* **2018**, *9*, 1–9.
  41. Grosjean, B.; Pean, C.; Siria, A.; Bocquet, L.; Vuilleumier, R.; Bocquet, M.-L. Chemisorption of Hydroxide on 2D Materials from DFT Calculations: Graphene versus Hexagonal Boron Nitride. *The Journal of Physical Chemistry Letters* **2016**, *7*, 4695–4700.
  42. Stecher, T.; Reuter, K.; Oberhofer, H. First-principles free-energy barriers for photoelectrochemical surface reactions: Proton abstraction at TiO<sub>2</sub> (110). *Physical Review Letters* **2016**, *117*, 276001.
  43. Duignan, T. T.; Kathmann, S. M.; Schenter, G. K.; Mundy, C. J. Toward a First-Principles Framework for Predicting Collective Properties of Electrolytes. *Accounts of Chemical Research* **2021**, 6131–6140.
  44. Baer, M. D.; Mundy, C. J. Toward an understanding of the specific ion effect using density functional theory. *The Journal of Physical Chemistry Letters* **2011**, *2*, 1088–1093.
  45. Schwierz, N.; Horinek, D.; Netz, R. R. Reversed anionic Hofmeister series: the interplay of surface charge and surface polarity. *Langmuir* **2010**, *26*, 7370–7379.
  46. Onsager, L. Reciprocal Relations in Irreversible Processes. I. *Physical Review* **1931**, *37*, 405–426.
  47. Onsager, L. Reciprocal Relations in Irreversible Processes. II. *Physical Review* **1931**, *38*, 2265–2279.
  48. Bocquet, L.; Barrat, J.-L. Flow boundary conditions from nano- to micro-scales. *Soft Matter* **2007**, *3*, 685–693.
  49. Marbach, S.; Bocquet, L. Osmosis, from molecular insights to large-scale applications. *Chemical Society Reviews* **2019**, *48*, 3102–3144.
  50. Anderson, J. L. Colloid transport by interfacial forces. *Annual Review of Fluid Mechanics* **1989**, *21*, 61–99.
  51. Mouterde, T.; Bocquet, L. Interfacial transport with mobile surface charges and consequences for ionic transport in carbon nanotubes. *The European Physical Journal E* **2018**, *41*, 148.
  52. Lee, C.; Cottin-Bizonne, C.; Biance, A.-L.; Joseph, P.; Bocquet, L.; Ybert, C. Osmotic Flow through Fully Permeable Nanochannels. *Physical Review Letters* **2014**, *112*, 244501.



53. Herrero, C.; Joly, L. Poisson-Boltzmann formulary. *arXiv preprint arXiv:2105.00720* **2021**,
54. Schoch, R.; Han, J.; Renaud, P. Transport phenomena in nanofluidics. *Reviews of Modern Physics* **2008**, *80*, 839–883.
55. McCaffrey, D. L.; Nguyen, S. C.; Cox, S. J.; Weller, H.; Alivisatos, A. P.; Geissler, P. L.; Saykally, R. J. Mechanism of ion adsorption to aqueous interfaces: Graphene/water vs. air/water. *Proceedings of the National Academy of Sciences* **2017**, *114*, 13369–13373.
56. Tocci, G.; Joly, L.; Michaelides, A. Friction of water on graphene and hexagonal boron Nitride from ab initio methods: very different slippage despite very similar interface structures. *Nano Letters* **2014**, *14*, 6872.
57. Tocci, G.; Bilichenko, M.; Joly, L.; Iannuzzi, M. *Ab initio* nanofluidics: disentangling the role of the energy landscape and of density correlations on liquid/solid friction. *Nanoscale* **2020**, *12*, 10994–11000.
58. Petrache, H. I.; Zemb, T.; Belloni, L.; Parsegian, V. A. Salt screening and specific ion adsorption determine neutral-lipid membrane interactions. *Proceedings of the National Academy of Sciences* **2006**, *103*, 7982–7987.
59. Lee, C.; Cottin-Bizonne, C.; Fulcrand, R.; Joly, L.; Ybert, C. Nanoscale Dynamics versus Surface Interactions: What Dictates Osmotic Transport? *The Journal of Physical Chemistry Letters* **2017**, *8*, 478–483.
60. Härtel, A.; Janssen, M.; Samin, S.; van Roij, R. Fundamental measure theory for the electric double layer: implications for blue-energy harvesting and water desalination. *Journal of Physics: Condensed Matter* **2015**, *27*, 194129.
61. Netz, R. R. Electrostatics of counter-ions at and between planar charged walls: From Poisson-Boltzmann to the strong-coupling theory. *The European Physical Journal E* **2001**, *5*, 557–574.
62. Kardar, M.; Golestanian, R. The “friction” of vacuum, and other fluctuation-induced forces. *Reviews of Modern Physics* **1999**, *71*, 1233.
63. Secchi, E.; Niguès, A.; Jubin, L.; Siria, A.; Bocquet, L. Scaling behavior for ionic transport and its fluctuations in individual carbon nanotubes. *Physical Review Letters* **2016**, *116*, 154501.
64. Grosjean, B.; Bocquet, M.-L.; Vuilleumier, R. Versatile electrification of two-dimensional nanomaterials in water. *Nature Communications* **2019**, *10*, 1656.
65. Biesheuvel, P.; Bazant, M. Analysis of ionic conductance of carbon nanotubes. *Physical Review E* **2016**, *94*, 050601.
66. Mouterde, T.; Keerthi, A.; Poggioli, A.; Dar, S. A.; Siria, A.; Geim, A. K.; Bocquet, L.; Radha, B. Molecular streaming and its voltage control in Ångström-scale channels. *Nature* **2019**, *567*, 87–90.
67. Secchi, E.; Marbach, S.; Niguès, A.; Stein, D.; Siria, A.; Bocquet, L. Massive radius-dependent flow slippage in carbon nanotubes. *Nature* **2016**, *537*, 210–213.
68. Van Itallie, C. M.; Anderson, J. M. Claudins and epithelial paracellular transport. *Annual Review of Physiology* **2006**, *68*, 403–429.
69. Van Itallie, C. M.; Fanning, A. S.; Anderson, J. M. Reversal of charge selectivity in cation or anion-selective epithelial lines by expression of different claudins. *American Journal of Physiology-Renal Physiology* **2003**, *285*, F1078–F1084.
70. Wang, L.; Wang, Z.; Patel, S. K.; Lin, S.; Elimelech, M. Nanopore-Based Power Generation from Salinity Gradient: Why It Is Not Viable. *ACS Nano* **2021**, *15*, 4093–4107.

71. Kühne, T. D.; Iannuzzi, M.; Del Ben, M.; Rybkin, V. V.; Seewald, P.; Stein, F.; Laino, T.; Khaliullin, R. Z.; Schütt, O.; Schiffmann, F., *et al.* CP2K: An electronic structure and molecular dynamics software package-Quickstep: Efficient and accurate electronic structure calculations. *The Journal of Chemical Physics* **2020**, *152*, 194103.
72. Klimeš, J.; Bowler, D. R.; Michaelides, A. Van der Waals Density Functionals Applied to Solids. *Physical Review B* **2011**, *83*, 195131.
73. Klimeš, J.; Bowler, D. R.; Michaelides, A. Chemical Accuracy for the van der Waals Density Functional. *Journal of Physics: Condensed Matter* **2010**, *22*, 022201.
74. Joly, L.; Tocci, G.; Merabia, S.; Michaelides, A. Strong Coupling between Nanofluidic Transport and Interfacial Chemistry: How Defect Reactivity Controls Liquid–Solid Friction through Hydrogen Bonding. *The Journal of Physical Chemistry Letters* **2016**, *7*, 1381–1386.
75. Graziano, G.; Klimeš, J.; Fernandez-Alonso, F.; Michaelides, A. Improved description of soft layered materials with van der Waals density functional theory. *Journal of Physics: Condensed Matter* **2012**, *24*, 424216.
76. Gillan, M. J.; Alfè, D.; Michaelides, A. Perspective: How good is DFT for water? *The Journal of Chemical Physics* **2016**, *144*, 130901.
77. Brandenburg, Jan Gerit and Zen, Andrea and Fitzner, Martin and Ramberger, Benjamin and Kresse, Georg and Tsatsoulis, Theodoros and Grüneis, Andreas and Michaelides, Angelos and Alfè Dario, Physisorption of water on graphene: Subchemical accuracy from many-body electronic structure methods. *The Journal of Physical Chemistry Letters* **2019**, *10*, 358–368.
78. Al-Hamdani, Y. S.; Ma, M.; Alfè, D.; von Lilienfeld, O. A.; Michaelides, A. Communication: Water on hexagonal boron nitride from diffusion Monte Carlo. *The Journal of Chemical Physics* **2015**, *142*, 181101.
79. Torrie, G. M.; Valleau, J. P. Nonphysical sampling distributions in Monte Carlo free-energy estimation: Umbrella sampling. *Journal of Computational Physics* **1977**, *23*, 187–199.
80. Kästner, J. Umbrella sampling. *Wiley Interdisciplinary Reviews: Computational Molecular Science* **2011**, *1*, 932–942.

# Graphical TOC Entry

